Control techniques with system efficiency comparison for micro-wind turbines

Danilo X Llano and Richard A McMahon

Abstract—**This paper presents the implementation of a sensorless speed controller and active rectification in a micro-wind turbine intended for battery charging. The controller was tested in a wind turbine emulator test rig using real wind data available from British bases in Antarctica. The control algorithm was successfully tested up to 14 m/s wind speed. Beyond this point the electrical unbalance in the turbine generator compromised the stability and performance of the system.**

Also, a system efficiency comparison of different control algorithms is given to demonstrate the advantages of using active rectification instead of passive diode rectifiers in micro-wind turbines. This comparison was done between the sensorless control plus active rectifier, a DC-DC converter regulator and the direct connection between the turbine and battery by means of a diode rectifier. The turbine with an active rectifier and sensorless control achieved the highest power coefficient over the range of wind speeds showing that this technique is an attractive and relatively low cost solution for maintaining good performance of micro-wind turbines at low and moderate wind speeds.

Index Terms—**Micro wind turbine, wind emulator test-rig, active rectification, sensorless speed control.**

I. Introduction

MICRO-wind turbines intended for battery charging have been used for decades. Indeed, they were the most commonly available devices (in limited numbers) in the wind energy market before the first oil price shock in early 1970s. After that crisis there was increasing interest and financial support in different countries such as Germany, Denmark, Sweden and the US to develop reliable and efficient large wind turbines (MW range) for power generation. The main aim at that time was looking at the diversification of power sources and reducing the dependency on fossil fuels coming from third party countries [1]. Micro-wind turbines have also been developed since then, with better aerodynamical design, more efficient electrical generators, improved materials and manufacturing processes. However, the power conversion stage has not changed significantly; passive rectification and DC to DC converters are the industry standard in micro-wind turbines [2].

Danilo X Llano was with the Electrical Engineering Division, University of Cambridge, 9 JJ Thompson CB3 0FA, Cambridge - UK. He is now with the Warwick Manufacturing Group, University of Warwick, Coventry CV4 7AL (email:dxl20@cantab.net / danilo.llano@gmail.com)

Richard A McMahon was with the Electrical Engineering Division, University of Cambridge, 9 JJ Thompson CB3 0FA, Cambridge - UK. He is now with the Warwick Manufacturing Group, University of Warwick, Coventry CV4 7AL (R.McMahon.1@warwick.ac.uk)

Some micro-wind turbines can be directly connected to a lead acid battery but this is not recommended by most of the manufacturers because the system does not have any control over charging. The battery can experience excessive charge rates and overcharging, which might lead to permanent damage. Manufacturers usually sell the turbine with a controller. The standard topology is a boost/buck converter to manage the battery charging cycle and a dump resistor to dissipate excess energy as heat if required (when the battery is fully charged). Otherwise, if the turbine is unloaded and the wind is blowing, the turbine will accelerate uncontrollably to high rotational speeds that could lead to damage [3]–[5].

Active rectification has not been explored at this power level (up to 250 W), presumably due to the extra costs associated with an active rectifier, its controller and sensors, and higher complexity in electronics and control algorithms. In addition, some micro-wind turbines have a built-in diode rectifier and then the DC power is transmitted via slip rings and brushes mounted on the turbine post. This mechanical arrangement enables passive yaw control by a tail blade that allows the turbine to align itself with the wind direction for better performance, but limits any chance of installing an active rectifier without providing an additional slip ring.

Aside from mechanical constraints, sensorless speed control and active rectification are an attractive option for micro-wind turbines from the economic and energy production points of view. The significant cost of the speed sensor (usually an optical encoder) is completely eliminated. The price of voltage and current sensors is also reduced since low-cost voltage dividers and shunt resistors can be straightforwardly used as sensors at this power range. In addition, relatively high performance microcontrollers (for running digital control algorithms), medium power MOSFETs and their drivers (for the active rectifier) are available in the market at competitive prices. Micro-wind turbines can achieve relatively high shaft speeds (up to 1500 RPM) at a terminal voltage suitable for connection to a 12 or 24 V battery [4], [5], so that MOSFETs are suitable switching devices.

Sensorless speed control is indeed technically challenging and not completely understood and developed for this particular application. In terms of control and speed estimation algorithms, a robust and reliable technique is required to compensate for the uncertainty in parameters, issues due to the machine construction, and varying and potentially harsh working conditions. Also, micro-wind turbines have fast dynamics since their mechanical inertia is much lower in comparison to medium or big wind turbines.

The main aim of this research is introducing means of cost-effective active rectification and sensorless speed control

for micro-wind turbines intended for battery charging and showing its increased performance and energy production in comparison to other control techniques. First, the turbine was exercised in a wind tunnel to estimate its performance parameters i.e. power coefficient and tip speed ratio and validate the proposed mathematical model. Then, the battery charging curves when the turbine is directly wired to a lead acid battery are provided as they are not given by manufacturers, but they are instrumental especially for understanding the dynamics of the system running without any electronic control (just the diode rectifier). These charging curves are also used in the efficiency comparison section. Later on, this paper describes the implementation of a sensorless speed controller for a micro-wind turbine with verification in an emulator test rig. Additionally, controller and system stability issues due to the unbalances in the generator are studied from an analytical and experimental approach to provide limiting working conditions. Finally, a system efficiency comparison of different control techniques was performed to show the advantages of active rectification in terms of overall power generation.

Common symbols used throughout the paper are presented in Table I.

Symbol	Description
L_{dq}	dq inductance
R_s	Phase resistance
ω_m	Rotor speed
J	Turbine Inertia
P	Pole-pairs
ϕ	Rotor flux
T_s	Sampling time
i_{dq}	dq stator currents
u_{dq}	dq stator voltages
C_p	Power coefficient
λ	Tip speed ratio
T_{em}	Electromagnetic torque
T_L	Load torque (wind torque)

Table I: Common Symbols

II. RUTLAND 913 WIND TURBINE

The wind turbine chosen for this study was a Rutland 913 model. This micro-wind turbine is widely available in the market and specifically designed for battery charging. It is a six bladed, horizontal axis, turbine based on a direct drive PM generator, without active pitch or yaw control. The generator is a three phase, star connected, axial flux, permanent magnet machine. Equations (1) and (2) describe the PM generator in the dq reference frame [6]

$$u_d = R_s i_d + L_d \frac{di_d}{dt} - L_q i_q P \omega_m \quad (1)$$

$$u_q = R_s i_q + L_q \frac{di_q}{dt} + L_d i_d P \omega_m + P \omega_m \phi \quad (2)$$

The terms $-L_q i_q P \omega_m$ in (1) and $L_d i_d P \omega_m + P \omega_m \phi$ in (2) are coupling terms.

An approximate model for the power coefficient, C_P, of the Rutland turbine is given by (3)

$$C_P = 0.2178 \left(\frac{64.8141}{\lambda_i} - 7.1916 \right) e^{-8.2844/\lambda_i} \quad (3)$$

with

$$\frac{1}{\lambda_i} = \frac{1}{\lambda} - 0.035 \quad (4)$$

It is assumed that the turbine blades are aligned with the wind direction due to the passive yaw control (tail blade).

Table II summarises the most important parameters of the turbine and its generator. The electrical parameters were estimated from tests and the performance parameters were estimated from wind tunnel measurements as described in subsection IV-A. The convention in [7], [8] was used, where the d-axis is aligned with the magnets, therefore $L_q > L_d$.

Parameter	value
Phase resistance (R_s)	0.8 Ω
Direct inductance (L_d)	0.87 mH
Quadrature inductance (L_q)	1.31 mH
Voltage constant (k_v)	45.2 mVp/RPM (mean value)
Pole pairs (P)	4
Maximum power coefficient ($C_p max$)	0.25 (mean value)
Optimal tip speed ratio (λ_{opt})	3.75 (mean value)
Blade radius (r)	0.455 m
Rated power (maximum)	250 W

Table II: Wind turbine specifications

III. EMULATOR TEST-RIG

A micro-wind turbine emulator test rig has been built up to replicate the behaviour of a real wind turbine [9], [10]. The prime mover is a servomotor rated at 3000 RPM, 19 Nm and 4.5 kW. It is controlled with an industrial drive and a target machine manufactured by Speedgoat that executes in real time the micro-wind turbine model described by (3) which is implemented in MATLAB/Simulink. A torque & speed transducer and an encoder are also included. Fig. 1 and 2 show the test rig diagrammatically and its physical realisation respectively.
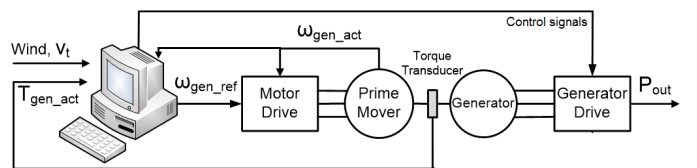
Figure 1: Test rig scheme

IV. TURBINE CHARACTERISATION AND CONTROL

First, the turbine was mounted in a wind tunnel and loaded with a variable resistor to estimate its maximum power coefficient at different wind speeds. Later on, three different strategies to operate the wind turbine were explored: direct connection to a lead acid battery, a power limiting controller developed by the British Antarctic Survey (BAS) for deployment in Antarctica and sensorless speed control and MOSFET based active rectifier. All these strategies can be straightforwardly applied to the PM generators commonly used in micro-wind turbines.

Figure 2: Test rig set up

Figure 4: Wind tunnel measurements

A. Wind tunnel measurements

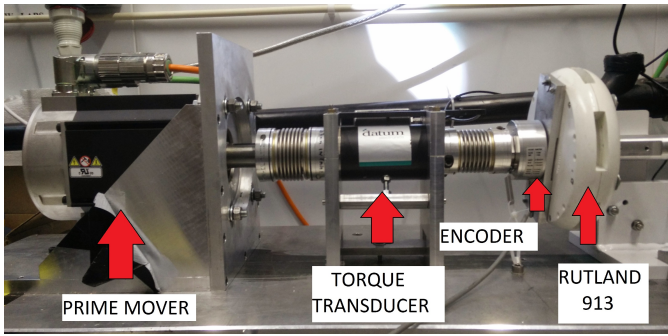The Rutland 913 wind turbine was installed in a wind tunnel to measure the power coefficient versus tip speed ratio curves at various wind speeds. Fig. 3 shows the setup. The experiment was carried out as follows: the wind turbine was aligned with the wind direction. The turbine has a built-in diode rectifier that was loaded by a variable resistance. The wind speed was set by the tunnel and the operating point was changed with the variable load resistance. The shaft speed was found from the frequency of the line voltage measured with a differential probe and oscilloscope. Power and shaft speed were recorded at various operational points for different wind speeds. The correction factors proposed in [11], [12] were applied to take into account the tunnel blockage due to the tunnel walls.

Figure 3: Wind tunnel setup

Fig. 4 shows the power coefficient versus tip speed ratio curves of the Rutland turbine at different wind speeds measured in the wind tunnel. The measurement points at different wind speeds present a noticeable trend which matches the model described in (3).

B. Turbine directly wired to a lead acid battery

The Rutland 913 turbine has a built-in three phase diode rectifier that was directly wired to two lead acid batteries connected in parallel to match the battery specification given by the turbine manufacturer. The batteries are Yuasa series NP-712 rated at 12 V - 7 Ah. The turbine was mounted in the wind tunnel to maintain constant wind speed during the entire charging cycle. The experiment was done as follows: the batteries were discharged to the minimum value recommended
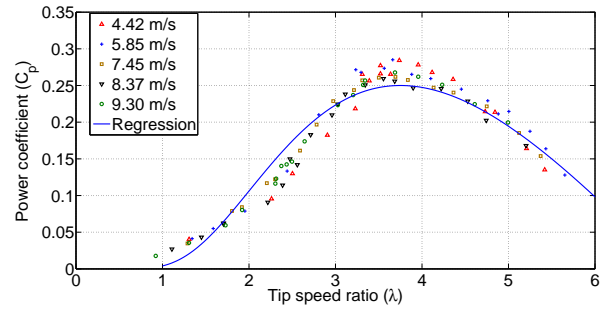
by the manufacturer. Then, the wind speed was set by the wind tunnel and the power coefficient and tip speed ratio of the turbine were recorded until the battery was fully charged. The battery was discharged and afterwards the experiment was repeated at a different wind speed. Fig. 5 shows the power coefficient of the turbine while charging the battery as a function of time (charge level) for different wind speeds. Fig. 6 presents the battery voltage as a function of time for different wind speeds. It may be seen that there is a significant increase in the charging rate when the battery voltage reaches about 13.5 V. This rise is consistent with the increment in power coefficient observed in Fig. 5, especially at higher wind speeds. At higher wind speeds more power is available, therefore the time required to fully charge the battery is shorter. High charging rates need to be carefully managed as they can damage the battery. During this experiment, voltages above 14.5 V were limited only to short periods of time.
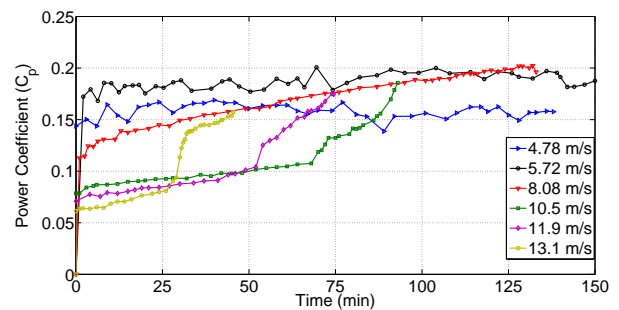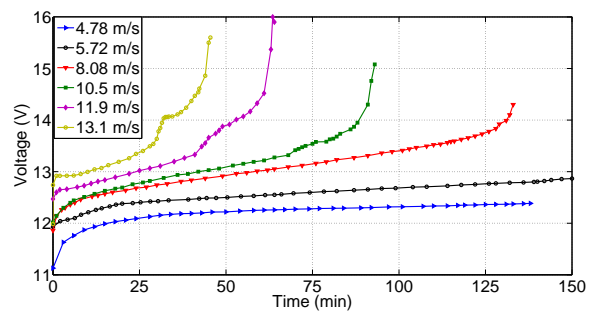

Figure 5: Battery charging waveforms

Figure 6: Battery voltage for different wind speeds

C. BAS controller

This controller was developed by BAS for micro-wind turbines in Antarctica [13], [14]. The controller was intended for robustness and reliability rather than efficiency. The controller is based on a passive diode rectifier connected to a switching MOSFET across the DC line to limit the DC voltage and current [15]. The maximum values at the output are 18 V and 5 A with 0.5 V and 0.5 A hysteresis bands respectively. The input current is limited to 12 A (average) and 15 A (peak). In case the output current and/or voltage exceed these values a PWM controlled MOSFET short-circuits the diode rectifier output to slow down the generator and limit the power output. The PWM switching frequency is 18 kHz and the duty cycle is updated at 23 Hz. When the variables are within the ranges the MOSFET is off. A second MOSFET is included as a "last resort" when the output voltage is higher than 20 V. This MOSFET connects a dump resistor across the diode bridge terminals.

V. SENSORLESS SPEED CONTROLLER

A. Unbalanced phases in the generator

The Rutland 913 turbine is a three phase, star connected (with no access to the neutral point), permanent magnet generator. Different measurements highlighted that the turbine is not properly balanced. Fig. 7 shows the open circuit back emf versus speed curves for each phase to phase combination. It can be observed that the slope is not the same in each case (43.3, 45.2 and 47.4 mV/RPM), and the absolute difference among phases is more significant at higher shaft speeds. Three different turbines were tested with fairly similar results, therefore it was possible to discard the suggestion that the differences were due to damage.
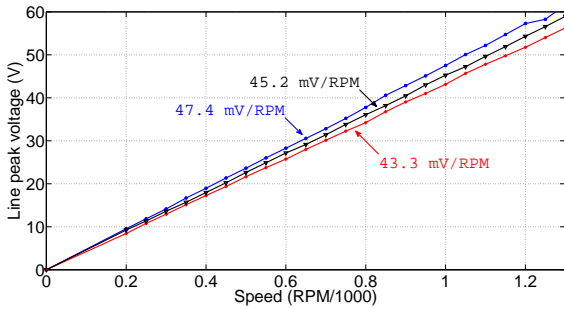

Figure 7: Voltage constant in the Rutland turbine

The phase unbalance is challenging when using active rectification because second order harmonics are produced in the DC link and this is reflected back in the machine in the form of triplen harmonics in the phase currents [16], [17]. These harmonics not only increase the losses in the generator but also compromise the stability of the controllers; especially because the dq variables, which are expected to be DC, have significant harmonic content.

B. Control scheme

A MOSFET based active rectifier, the advanced sensorless estimation technique and maximum power point tracking

(MPPT) algorithms presented in [18] were used to control the wind generator near its optimal point regardless of the wind conditions. The generator and turbine parameters were changed to match the Rutland turbine characteristics but most of the control and estimation tuning parameters remained the same. Fig. 8 shows the sensorless control diagram and main hardware components. The $H\infty$ filter is used to calculate the shaft speed and position (necessary for the Park transformation) and a Luenberger observer estimates the wind torque. The phase currents, which are measured with Hall effect sensors (CKSR 6-NP current transducer from LEM), and the control voltages (output signals from the inner PI controller which are fed to the SVPWM block) are used to estimate the speed, position and torque. The MPPT algorithm sets the speed reference to operate the turbine near its optimal working point regardless of the wind conditions. The outer PI controller tracks the speed reference by setting the I_q reference current for the inner PI controller. The latter controller block will create the control voltages V_{dq} to drive the active rectifier accordingly. The control scheme described in this section has the same structure as the technique in [18], but applied to a micro-wind turbine generator designed for passive rectification and battery charging. Obviously, the being tested generator imposes the need for new machine parameters and control gains in controllers and estimators. Further details on the hardware, control blocks and algorithms are given in the following subsections.
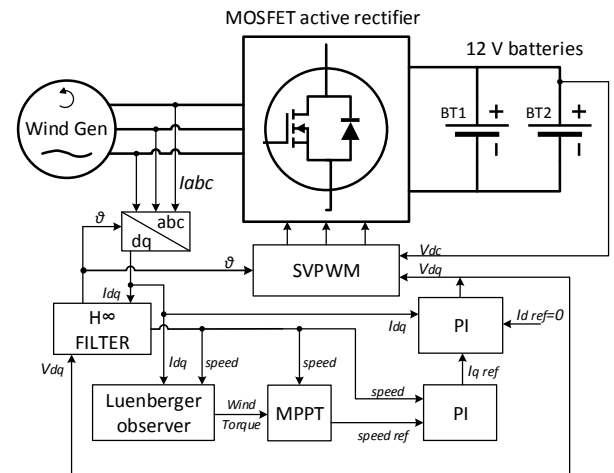
Figure 8: Sensorless control scheme

1) MOSFET active rectifier: Fig. 9 shows one leg of the MOSFET active rectifier. A digital isolator ISO7420FE, IR2110 gate driver and IRFP064N MOSFETs are the key components. The remaining components were selected based on the manufacturer application notes.

The control system comprises of various functional blocks that are explained as follows.

2) Extended $H\infty$ filter: The extended $H\infty$ filter is a robust algorithm intended to estimate states or parameters in non linear systems and its sequence is detailed in Algorithm 1.

Figure 9: Circuit diagram for the active rectifier - one leg

Algorithm 1 Extended H∞ Filter [19]–[21]

$$X[k|k-1] = f(x(k), u(k), k)$$
$$P[k|k-1] = \Phi[k-1]P[k-1|k-1]\Phi^T[k-1] + Q[k-1]$$

$$K[k] = P[k|k-1]\overline{H}^T[k] \cdot$$
$$\left(\overline{H}[k]P[k|k-1]\overline{H}^T[k] + R[k]\right)^{-1}$$

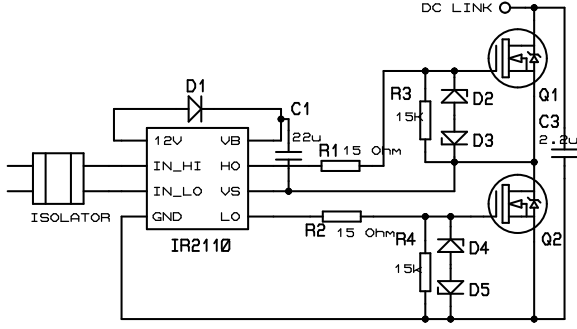$$X[k|k] = X[k|k-1] + K[k]\left(Y[k] - \bar{H}[k]X[k|k-1]\right)$$

$$P[k|k] = P[k|k-1] - P[k|k-1] \cdot$$
$$\left(\begin{array}{cc} \overline{H}^T[k] & L^T[k] \end{array}\right) R_e^{-1}[k] \cdot$$
$$\left(\begin{array}{c} \overline{H}[k] \\ L[k] \end{array}\right) P[k|k-1]$$

$$R_e[k] = \left(\begin{array}{cc} R_{e11}[k] & R_{e12}[k] \\ R_{e21}[k] & R_{e22}[k] \end{array}\right)$$

$$R_{e11}[k] = R + \overline{H}[k] P[k|k-1] \overline{H}^T[k]$$

$$R_{e12}[k] = \overline{H}[k] P[k|k-1] L^T[k]$$

$$R_{e21}[k] = L[k] P[k|k-1] \overline{H}^T[k]$$

$$R_{e22}[k] = -\gamma^2 I + L[k] P[k|k-1] L^T[k]$$

where Φ is defined as:

$$\Phi[k] \approx \left.\frac{\partial f(x(k), u(k), k)}{\partial x}\right|_{X(k|k)}$$

The notation $\Gamma[n|m]$ in Algorithm 1 means the value of the matrix Γ at instant n taking into account m previous updates.

The extended H∞ filter equations were written by using (1) and (2), the speed ω_m modelled as a perturbation so that

$$\omega_m[k] \approx \omega_m[k-1] \quad (5)$$

and the relationship between the electrical angle θ_e and the mechanical speed ω_m

$$\theta_e[k] = \theta_e[k-1] + PT_s\omega_m \quad (6)$$

The corresponding extended H∞ filter equations for the PM generator are written below:

$$f(x(k), u(k), k) = \quad (7)$$

$$\left(\begin{array}{c} (1 - R_sT_s/L_s)\,i_d + PT_s\omega_m i_q + \frac{T_s}{L_s}u_d \\ -PT_s\omega_m i_d + (1 - R_sT_s/L_s)\,i_q - P\omega_m\phi\frac{T_s}{L_s} + \frac{T_s}{L_s}u_q \\ \omega_m \\ PT_s\omega_m + \theta_e \end{array}\right)$$

$$X[k] = \left[\begin{array}{cccc} i_d & i_q & \omega_m & \theta_e \end{array}\right]^T \quad (8)$$

$$Y[k] = \left[\begin{array}{cc} i_d & i_q \end{array}\right]^T \quad (9)$$

$$\overline{H}[k] = \left[\begin{array}{cccc} 1 & 0 & 0 & 0 \\ 0 & 1 & 0 & 0 \end{array}\right] \quad (10)$$

$$L = \left[\begin{array}{cccc} 1 & 0 & 0 & 0 \\ 0 & 1 & 0 & 0 \end{array}\right] \quad (11)$$

$$\Phi = \left[\begin{array}{cccc} 1 - \frac{R_sT_s}{L_s} & PT_s\omega_m & PT_s i_q & 0 \\ -PT_s\omega_m & 1 - \frac{R_sT_s}{L_s} & -PT_s i_d - \frac{PT_s\phi}{L_s} & 0 \\ 0 & 0 & 1 & 0 \\ 0 & 0 & PT_s & 1 \end{array}\right] \quad (12)$$

$$Q[k] = diag\left(\begin{array}{cccc} 0.05 & 0.05 & 0.05 & 0.015 \end{array}\right) \quad (13)$$
$$R[k] = 0.21 \times diag(2 \times 2) \quad (14)$$
$$\gamma^2 = 0.08 \quad (15)$$

$Q[k]$, $R[k]$ and γ were tuned according to the application requirements and simulation results.

3) Torque estimator : The estimated load torque $\hat{T}_L$ corresponds to the wind turbine torque T_{wind}, as a consequence it is unknown and uncontrolled. A Luenberger observer was proposed to calculate $T_L = T_{wind}$. It uses the speed and current to estimate the wind torque.

$$\hat{\omega}_m[k+1] = \hat{\omega}_m[k] - \frac{3}{2}\frac{PT_s}{J}\phi i_q[k]$$

$$+ \frac{T_s\hat{T}_L[k]}{J} + \alpha_{L1}T_s\left(\omega_m[k] - \hat{\omega}_m[k]\right) \quad (16)$$

$$\hat{T}_L[k+1] = \hat{T}_L[k] + \alpha_{L2}T_s\left(\omega_m[k] - \hat{\omega}_m[k]\right) \quad (17)$$

The variables with the index "∧" are estimated values and variables without a super index are measured values.

T_s is the sampling time

α_{L1} and α_{L2} are gains set to guarantee fast convergence of the estimation. $\alpha_{L2} = \frac{J}{4}\alpha_{L1}^2$

Details about the design of the Luenberger observer are given in [22]

4) Maximum power point tracking algorithm: The expected power output of a wind turbine can be written as:

$$P_m = C_p \frac{\rho \pi r^5}{2\lambda^3} \omega_m^3 \qquad (18)$$

where ρ is the air density, r is the turbine blade radius, ω_m is the rotor speed, C_p is the power coefficient and λ is the tip speed ratio defined as:

$$\lambda = \frac{\omega_m r}{v} \qquad (19)$$

v is the wind speed.

C_p and λ have both optimal values that depend on the turbine characteristics and are usually provided by manufacturers or estimated from tests (the latter for this paper). The wind turbine emulator test-rig used in this paper has the following mechanical parameters: $\rho = 1.225$ kg.m^{-3}, $r = 0.455$ m, $C_P opt = 0.25$ and $\lambda opt = 3.75$ as listed in Table II.

The mechanical torque T can be written as $T = P_m/\omega_m$. In wind turbines, by taking $C_p opt$, λopt and (18)

$$T = C_p opt \frac{\rho \pi r^5}{2\lambda opt^3} \omega_{opt}^2 \qquad (20)$$

Since all the parameters in (20) are constant, for a given torque T, there is an optimal shaft speed ω_{opt} to achieve maximum power extraction. This strategy was used in [9], but the wind torque was measured with a bulky torque transducer. In this paper T is estimated as $\hat{T}_L$ using a Luenberger observer so it can be used to set the optimal speed reference ω_{opt}. To deal with noise, numerical errors and changing wind conditions the following iterative algorithm is proposed:

1) Wait 10 s after the last speed reference update because the system response is relatively slow, compared to a standard PM motor, due to the inertia in the turbine and there is no motoring operation.

2) Take samples of the estimated torque $\hat{T}_L$ for 10 s each 0.2 s. Average those samples to get the mean value $\bar{T}_L$.

3) Calculate the optimal speed reference by using $\bar{T}_L$ in (20) and set ω_{opt} as the new speed reference.

4) Return to step one.

5) Further considerations: As already stated, the Rutland generator is an unbalanced machine and some modifications in the control scheme were required to address this problem. The authors in [16], [17] considered an inverter tied to an unbalanced grid. They addressed the unbalance in the system by using notch filters centred at the grid frequency (50 Hz). This solution cannot be applied in this case because the frequency varies with the generator speed. In this present paper, low pass filters were used to filter out high frequency components due to the unbalance in the generator, but stability problems and reduced bandwidth of the controllers are the drawbacks of this technique. The stability margin decreases if the cut-off frequency is reduced as shown in the next section.

C. Stability of the system

Fig. 10 shows the block diagram of the generator and control system in the dq reference frame including approximations for the delays due to ADC sampling, control algorithm execution and the PWM active rectifier as proposed in [23], [24]. PI controllers are used in the block diagram representation because they are commonly used in wind turbine control, their transfer function is straightforward to write in the Laplace variable and simplifies the stability analysis of the system. Fig. 10a shows the control diagram of the i_{dq} currents. The coupling terms in (1) and (2) are compensated using the decoupling terms $L_q i_q P \omega_m$ and $-L_d i_d P \omega_m - P \omega_m \phi$ for the d and q axis respectively. The decoupling terms are directly added to the control voltages feeding the active rectifier. This simplifies the stability analysis and allows evaluating the d and q axis independently. After the compensation stage, the coupling terms are approximated as disturbances and not included in the block diagram for the stability analysis.

Low pass filters (LPF) were included in the control loop for removing unwanted harmonics from measured signals, especially due to the unbalance in the generator, but these filters also reduced the bandwidth of the controller. A trade-off between stability and performance was necessary. The plant in Fig. 10 was numerically analysed in Simulink using Matlab's Sisotool toolbox to obtain the Bode diagrams of the system and establish the controller gains using the criteria presented in [25]. Later on, these gains were used as initial values for a detailed simulation implemented in Simulink using its SimPower library. This simulation model included the wind turbine dynamics, estimators and power electronics. The gains obtained with the detailed simulation model were used in the experimental implementation.

The $H\infty$ filter was not included in the stability analysis as it is well known that this filter becomes unstable near zero speed, which is important in motoring mode, but in this application, the generator is started by the blades (prime mover) using passive rectification with the body diodes of the active rectifier to avoid problems at low speed. Also, wind turbines have a cut-in wind speed (around 2.4 m/s) where they start to operate. Near zero operational speeds are therefore unlikely.

Fig. 10b shows the control diagram of the speed. The inner "current loop" block represents the diagram in Fig. 10a for the i_q current controller. The load torque T_L was included as a disturbance in Fig. 10b, but it was not considered for the stability analysis.

Discrete time pole-zero maps of the system using different cut-off frequencies for the low pass filters were plotted to explore the stability of the current and speed control loops. The Tustin approximation was used as discretization method with $T_s = 400$ μs.

Fig. 11 shows the pole-zero map for the speed control loop. Fig. 12 shows a zoomed-in view of the most important poles in the map. It can be observed how the dominant poles (the Xs closer to the unit circle border on the right side of the figure) move when the cut-off frequency of the low pass filters is changed. The control parameters were chosen to have all the poles (Xs) inside the unit circle and assure the stability of
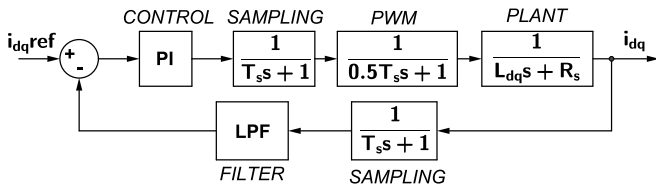
(a) dq current
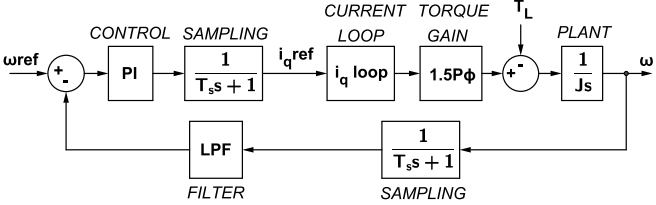
(b) Speed

Figure 10: Block diagrams of the system

the system. It can be also seen that if the cut-off frequency of the low pass filters is reduced, then the dominant poles approach to the border of the unit circle (as indicated by the arrow), therefore the stability margin is effectively reduced. The same behaviour was observed in the pole-zero maps for the i_{dq} currents.
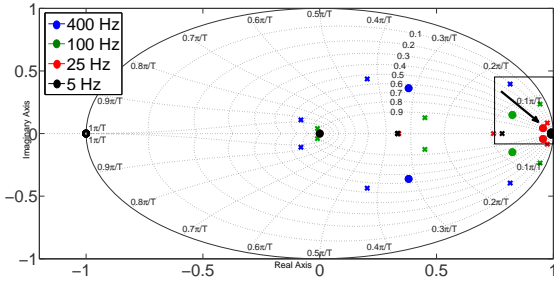

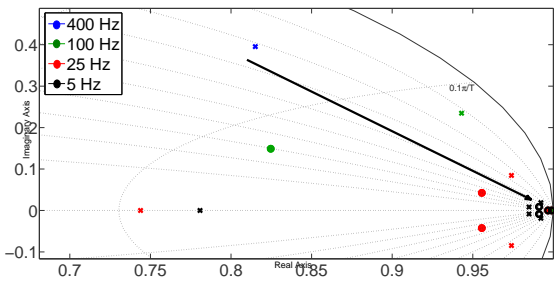Figure 11: Pole-zero map for the speed control loop

Figure 12: Pole-zero map for the speed control loop - zoomed-in view

VI. Experimental results

The wind speed profile shown in Fig. 13a was used to initially test the sensorless controller and MPPT algorithm. Fig. 13b shows the speed tracking needed to operate the

turbine near its maximum power coefficient (Fig. 13c) and optimal tip speed ratio (Fig. 13d).

The unbalance between phases is more significant as the rotational speed increases, leading to higher harmonic content in the dq variables, less effective low pass filters and finally the system becomes unstable. The power generation cannot be easily limited since there are no opportunities for yaw or pitch control as is the case in larger wind turbines. The wind speed profile shown in Fig. 14 was applied to the test rig. The steps in wind speed were used to identify the point where system becomes unstable. Fig. 15 shows that the controller was able to track the maximum power point regardless of the wind conditions, up to 14 m/s. The controller was tested with different gains, but the instability point was near 14 m/s in all the cases.
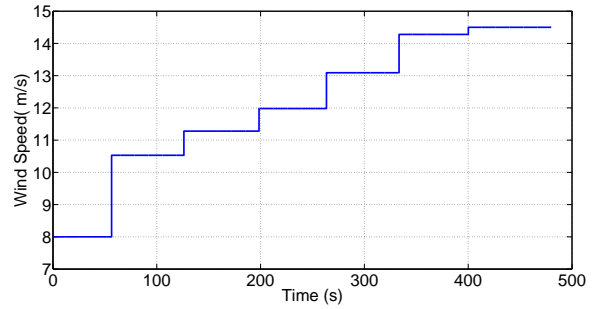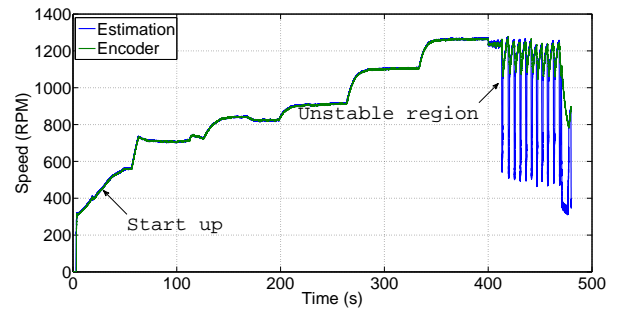

Figure 14: Wind speed profile

Figure 15: Unstable operation

VII. System efficiency comparison

This section presents a comparison of the system efficiency of different control techniques developed for micro-wind turbines. Fig. 16 shows power coefficient measurements at different wind speeds. In all the cases the wind speed was set constant either in the wind tunnel or in the emulator test rig and then the controller was operated for at least 10 minutes to record data. The power coefficient reported in this section corresponds to the average performance at each wind speed. The grey bars represent the maximum power coefficient measured in the wind tunnel without any controller, just by changing the turbine operation point with a variable resistor. The bars in red correspond to the BAS controller's performance. As expected, this approach was not particularly efficient, especially at high wind speeds. The power output

(a) Wind speed profile used for MPPT

(b) Speed tracking using MPPT

(c) Power coefficient using MPPT

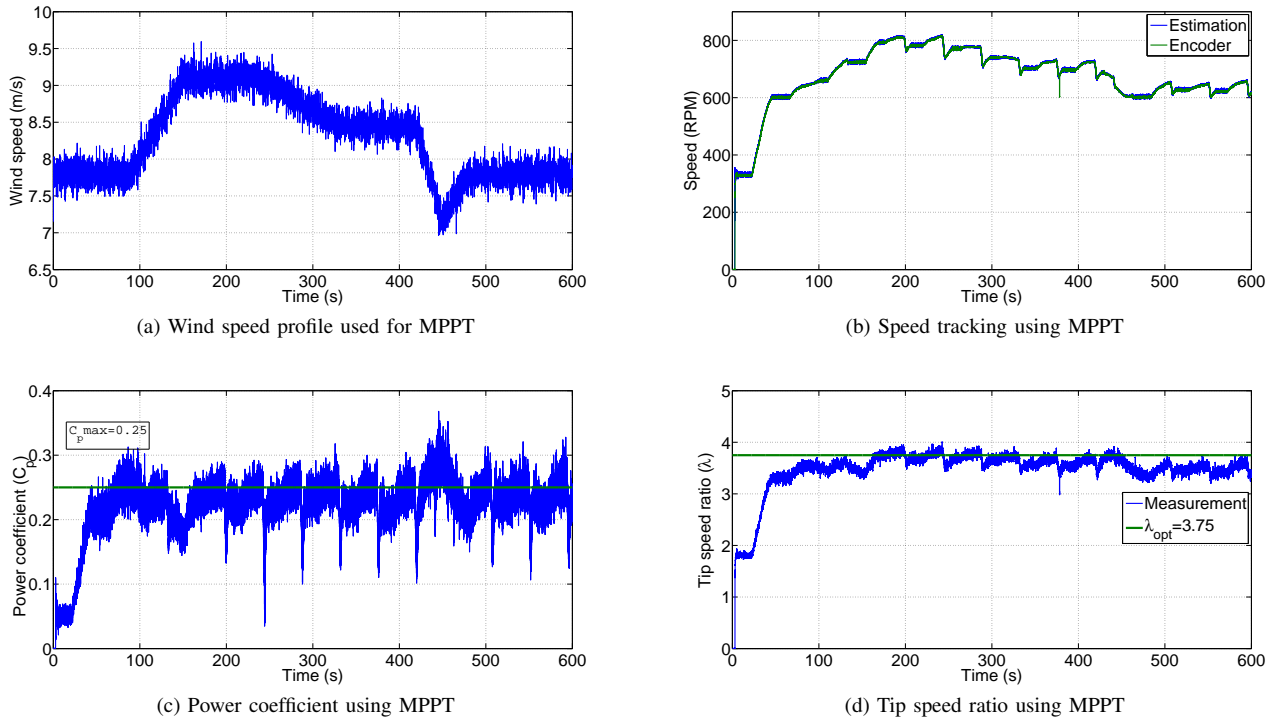(d) Tip speed ratio using MPPT

Figure 13: Sensorless speed control -Experimental results

of the BAS controller is limited to approximately 90 W regardless of the wind conditions. The blue bars are the power coefficient of the turbine directly connected to a lead acid battery. The turbine achieved a higher power coefficient when the battery was close to fully charged as it was shown in Fig. 5, but as already mentioned, the value reported on Fig. 16 corresponds to the average power coefficient. Finally, the green bars correspond to the power coefficient using sensorless control and active rectification. This technique has the highest power coefficient over the range of wind speeds, but the algorithm was stable only up to 14 m/s wind speed.
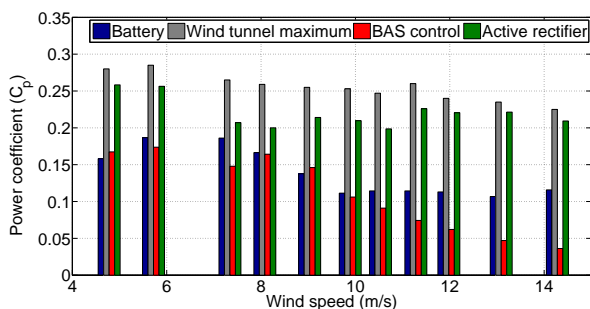

Figure 16: Efficiency comparison

VIII. CONCLUSIONS

The MPPT algorithm, $H\infty$ filter and PI controller developed for small scale wind turbines in [18] were applied to a micro-wind turbine (Rutland 913) intended for battery charging. The machine parameters of the controller and estimation algorithms were changed according to the values of the Rutland turbine. The combination of algorithms and estimators in the sensorless control system for the active rectifier showed fairly good performance up to 14 m/s wind speed, but above this point the system became unstable due to the unbalanced phases of the Rutland turbine. The unbalance in the turbine generator introduced unwanted harmonics in the DC link voltage and phase currents that need to be addressed. Low pass filters were used in this paper, but these filters limited the bandwidth and stability of the controller.

A comparison of the system efficiency of different configurations for the Rutland turbine was also given. The sensorless control with active rectification had the best performance. The turbine with the BAS controller had the lowest power coefficient but this controller was designed primarily for reliability and robustness. Connecting the turbine directly to a lead acid battery is the simplest solution, with fairly good performance at low wind speeds but protection against overcharging the batteries, for example, cannot be implemented in this configuration. The comparison of system efficiency indicates that sensorless speed control is an especially attractive control scheme when the device is operated at low to moderate wind speeds. It is worth mentioning that active rectification was tested with a regular wind turbine available in the market and designed for passive rectification, where the unbalance in the generator would not be a significant issue. Further research will be focused on improving the stability of the system and its controllers.

References

[1] R. I. of Technology Stockholm-Sweden, *Wind Power in Power Systems*, T. Ackerman, Ed. John Wiley & Sons, Inc., 2005.

[2] P. Gipe, *Wind power Renewable Energy for Home, Farm and Business*. Chelsea Green Publishing Company, 2004.

[3] *Catalogue of European Urban Wind Turbine Manufacturers*, European Commission under the Intelligent Energy Europe programme.

[4] *Rutland 913 Windcharger Owners Manual*, MARLEC, February 2013.

[5] *AMPAIR 100 Operation Installation & Maintenance Manual Manufactured by Ampair*, rev 1.3 ed., Ampair, October 2012.

[6] P. Vas, *Sensorless vector and direct torque control*, ser. Monographs in electrical and electronic engineering. Oxford University Press, 1998.

[7] J. Hendershot and T. Miller, *Design of Brushless Permanent-magnet Machines*. Motor Design Books, 2010. [Online]. Available: https://books.google.co.uk/books?id=n833QwAACAAJ

[8] H. Toliyat and G. Kliman, *Handbook of Electric Motors*, ser. Electrical and computer engineering. CRC Press, 2004. [Online]. Available: https://books.google.co.uk/books?id=4-Kkj53fWTIC

[9] M. Tatlow, "Wind Turbine Emulator System for Testing Small-Scale Wind Generators and Associated Power Electronics," Master's thesis, University of Cambridge, 2011.

[10] D. Llano, M. Tatlow, and R. McMahon, "Control algorithms for permanent magnet generators evaluated on a wind turbine emulator test-rig," in *Power Electronics, Machines and Drives (PEMD 2014), 7th IET International Conference on*, April 2014, pp. 1–7.

[11] T. Chen and L. Liou, "Blockage corrections in wind tunnel tests of small horizontal-axis wind turbines," *Experimental Thermal and Fluid Science*, vol. 35, no. 3, pp. 565 – 569, 2011. [Online]. Available: http://www.sciencedirect.com/science/article/pii/S0894177710002438

[12] F. Campagnolo, "Wind tunnel testing of scaled wind turbine models: Aerodynamics and Beyond," Ph.D. dissertation, Politecnico di Milano, 2013.

[13] M. C. Rose, "Variable speed wind generator control in Antarctica," *Geophysical Research Abstracts*, vol. 9, p. 02051, 2007.

[14] T. Tin, B. K. Sovacool, D. Blake, P. Magill, S. E. Naggar, S. Lidstrom, K. Ishizawa, and J. Berte, "Energy efficiency and renewable energy under extreme conditions: Case studies from Antarctica," *Renewable Energy*, vol. 35, no. 8, pp. 1715 – 1723, 2010. [Online]. Available: http://www.sciencedirect.com/science/article/pii/S0960148109004467

[15] D. M. Whaley, W. L. Soong, and N. Ertugrul, "Investigation of switched-mode rectifier for control of small-scale wind turbines," in *Industry Applications Conference, 2005. Fourtieth IAS Annual Meeting. Conference Record of the 2005*, vol. 4, Oct 2005, pp. 2849–2856 Vol. 4.

[16] L. Moran, P. Ziogas, and G. Joos, "Design aspects of synchronous PWM rectifier-inverter systems under unbalanced input voltage conditions," in *Industry Applications Society Annual Meeting, 1989., Conference Record of the 1989 IEEE*, Oct 1989, pp. 877–884 vol.1.

[17] S. Shao, T. Long, E. Abdi, and R. McMahon, "Dynamic Control of the Brushless Doubly Fed Induction Generator Under Unbalanced Operation," *Industrial Electronics, IEEE Transactions on*, vol. 60, no. 6, pp. 2465–2476, June 2013.

[18] D. Llano and R. McMahon, "Torque observer and extended H infinity filter for sensorless control of permanent magnet generators tested on a wind turbine emulator," in *Industrial Electronics Society, IECON 2015 - 41st Annual Conference of the IEEE*, Nov 2015, pp. 000 123–000 128.

[19] U. Shaked and N. Berman, "H infinity nonlinear filtering of discrete-time processes," *Signal Processing, IEEE Transactions on*, vol. 43, no. 9, pp. 2205–2209, Sep 1995.

[20] G. Einicke and L. White, "Robust extended Kalman filtering," *Signal Processing, IEEE Transactions on*, vol. 47, no. 9, pp. 2596–2599, Sep 1999.

[21] W. Li and Y. Jia, "H-infinity filtering for a class of nonlinear discrete-time systems based on unscented transform," *Signal Processing*, vol. 90, no. 12, pp. 3301 – 3307, 2010. [Online]. Available: http://www.sciencedirect.com/science/article/pii/S0165168410002252

[22] D. Llano, "Sensorless control techniques and associated power electronics for generators in micro and small-scale wind turbines," Ph.D. dissertation, University of Cambridge, July 2016.

[23] F. B. Marian Kazmierkowski, R. Krishnan, Ed., *Control in Power Electronics. Selected Problems*. Academic Press Series in Engineering, 2002.

[24] V. Blasko and V. Kaura, "A novel control to actively damp resonance in input LC filter of a three phase voltage source converter," in *Applied Power Electronics Conference and Exposition, 1996. APEC '96. Conference Proceedings 1996., Eleventh Annual*, vol. 2, Mar 1996, pp. 545–551 vol.2.

[25] K. Ogata, *Modern Control Engineering*. Prentice-Hall, 2010.

Danilo X Llano received the BSc. degree in Electronic Engineering from Universidad San Francisco de Quito, Ecuador, in 2012. He received the Ph.D. degree from the University of Cambridge, UK in July 2016. In October 2016, he joined WMG, at Warwick University, Coventry, UK, as a Research Fellow at the Advanced Propulsion Systems Group. His current research interests includes sensorless control of electrical drives, sensorless estimation algorithms, electrical machine and small wind turbine in MATLAB/Simulink, power electronics, wireless instrumentation, electric powertrain systems and sensor design.

Richard A McMahon received the B.A. degree in electrical sciences and the Ph.D degree in electrical engineering the University of Cambridge, UK, in 1976 and 1980, respectively. Following his Post-Doctoral research on semiconductor device processing, he was appointed as the University Lecturer in Electrical Engineering in the Engineering Department, Cambridge University, in 1989, and became a Senior Lecturer in 2000. In 2016, he joined WMG, at Warwick University, Coventry, UK, as a Professor of power electronics. His research interests include electrical drives, power electronics, and semiconductor materials.